
Sphere-Guided Training of Neural Implicit Surfaces

Andreea Dogaru¹Andrei Timotei Ardelean¹Savva Ignatyev¹Evgeny Burnaev^{1,2}Egor Zakharov¹¹ Skolkovo Institute of Science and Technology² Artificial Intelligence Research Institute

Abstract

In recent years, surface modeling via neural implicit functions has become one of the main techniques for multi-view 3D reconstruction. However, the state-of-the-art methods rely on the implicit functions to model an entire volume of the scene, leading to reduced reconstruction fidelity in the areas with thin objects or high-frequency details. To address that, we present a method for jointly training neural implicit surfaces alongside an auxiliary explicit shape representation, which acts as surface guide. In our approach, this representation encapsulates the surface region of the scene and enables us to boost the efficiency of the implicit function training by only modeling the volume in that region. We propose using a set of learnable spherical primitives as a learnable surface guidance since they can be efficiently trained alongside the neural surface function using its gradients. Our training pipeline consists of iterative updates of the spheres' centers using the gradients of the implicit function and then fine-tuning the latter to the updated surface region of the scene. We show that such modification to the training procedure can be plugged into several popular implicit reconstruction methods, improving the quality of the results over multiple 3D reconstruction benchmarks.

1 Introduction

The problem of multi-view 3D reconstruction has been one of the main areas of research in computer vision and graphics, and has applications in various practical areas, such as AR/VR metaverses, synthetic media, medical imaging, and computer animation. The de-facto standard tools in this area are represented by the multi-view reconstruction systems (MVS) [2, 3, 5, 7, 9, 26, 42], which estimate the underlying scene geometry using photometric consistency of the projected points between multiple views. Such methods can be made highly efficient both with respect to compute and memory, and, at the same time, are able to handle large amounts of data and scene sizes [6].

In recent years, there have been a surge in development of systems that directly optimize the scene geometry using neural rendering [4, 14, 16, 17, 18, 20, 22, 28, 33, 31, 35, 38, 39, 41] techniques, aimed at addressing the known limitations of classical methods, related to modeling of non-Lambertian and texture-less surfaces [6]. Among these approaches, neural implicit density and surface representations, trained using volume rendering [11], have gained the most attention. Such systems indeed have numerous advantages: they can represent arbitrary complex scene topologies, are continuous, and support large resolutions for the scene volume. However, they take notoriously long time to train and render since the volume rendering procedure requires multiple evaluations of the implicit function to obtain the color of each pixel.

This issue has been recognized and addressed in several previous and concurrent works [16, 18, 33, 35, 41], which combine the explicit data structures with the implicit functions into hybrid representations, achieving increased training and inference speeds for novel view synthesis problem. Similar hybrid

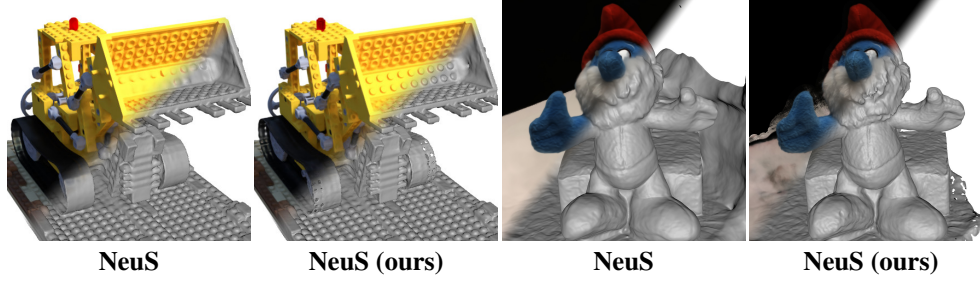


Figure 1: Our proposed solution enhances the training efficiency of neural implicit surfaces, which enables them to better represent the geometry of the underlying scenes, as well as achieve higher rendering quality. Digital zoom-in is recommended.

structures were also applied [33] to the surface reconstruction task, where they were shown to provide a boost in the quality of the results more so than the inference or training speeds.

In our method, we propose a number of improvements to the hybrid training approach, which further boost the accuracy of the resulting reconstructions. We accomplish this by training a guiding sphere cloud, and using it to improve both ray sampling *and* ray marching procedures of the volume rendering. Additionally, we propose using a sphere resampling scheme, which prevents them from getting stuck in the local minimas, as well as a repulsion mechanism, adaptive to the size of the spheres, ensuring high degrees of exploration of the object’s surface. Our last contribution is an empirical evidence of the proposed method’s applicability to different approaches for implicit surface modeling. To evaluate that, we pair our method with several modern systems [4, 22, 31, 38] for surface reconstruction and observe uniform improvements in the resulting quality across multiple 3D reconstruction benchmarks.

2 Related works

Multi-view stereo reconstruction Classic multi-view stereo (MVS) methods rely on explicit 3D representations to model the scene geometry, such as depth maps [2, 3, 9, 26], 3D point clouds [7], or triangle meshes [5]. The most prominent approach, COLMAP [26], estimates depth and normal maps for each training view via multi-view photo-consistency and then fuses them into a global point cloud. While highly efficient, this and other classical MVS methods are known to struggle [6] with modeling texture-less objects and objects with non-Lambertian surfaces, which make it hard to estimate pixel-wise descriptors both unique and consistent across multiple views. More recently, several Deep Learning based MVS methods have been proposed [37, 36, 19, 30] bringing significant improvements over classical methods in both quality and running time. Nonetheless, these methods are still limited in their applicability outside of the training domain [32]. Our method instead relies on the implicit surface representations to perform the reconstruction. These implicit functions are trained for each scene via volume rendering, and their radiance is parameterized by both location and viewing direction, which circumvents most of the photo-consistency issues faced by the classical methods.

Implicit neural representations In recent years, implicit neural representations have gained much attention in the areas of novel view synthesis, with Neural Radiance Fields (NeRFs) [20] system being the most well-known example. One of its key ideas is the usage of volume rendering, which was later adapted to the problem of surface reconstruction [4, 22, 38, 31] in the follow-up works. However, both volume and a simpler surface rendering [12, 39] approaches can converge to suboptimal reconstructions due to the poor choice of training samples. Iso-Points [33] method addresses this problem by oversampling the training rays near the object’s surface, which improves the reconstruction quality. In our approach, we go one step further than that and sample both the rays *and* points along these rays to lie near the surface, thus modifying both ray sampling and ray marching procedures. As we show in our experiments, updating the ray marching is crucial and leads to significant improvements in the reconstruction quality. This modification makes our proposed approach similar to the Neural Sparse Voxel Fields (NSVF) [16] novel view synthesis system, which utilizes sparse voxels to guide the ray marching procedure. In our work, we show that for the surface reconstruction problem, one can use the *gradient-based* optimization of the explicit representation, which enables

us to update it at each training iteration using a *single* forward-backward pass of the implicit function, instead of thousands of forward passes required by the NSVF method.

Neural rendering of the explicit surface representations Some methods, alternative to implicit modeling, have tackled the problem of novel view synthesis by combining explicit 3D structures with neural rendering. They either utilize depth maps [34], point clouds [1, 23, 25], volume primitives [14], triangle meshes [29, 24], or dense/sparse volumetric grids [17, 21, 40, 41], and have the advantage of higher training and inference speeds. However, some of these systems [1, 23, 29, 24] assume the availability of a high-quality geometry, while others focus on novel view synthesis, achieving subpar quality of 3D reconstructions [17, 21, 40, 41]. In our approach, we do not rely on the explicit representations for estimating the underlying geometry of the scene since achieving high reconstruction fidelity would make their training either computationally intractable or require large amounts of data. Instead, these representations act as a coarse approximation for the object’s surface and are used to guide the reconstruction via implicit representations.

3 Method

Our approach addresses a multi-view 3D reconstruction problem. The goal is to estimate the surface of a scene, denoted as \mathcal{S} , given a collection of images with the associated camera parameters. In our case, this surface is extracted as a level set of the learned implicit representations: either a signed distance function (SDF) or an occupancy field. In this section, we begin by describing the volume rendering approach utilized by most the state-of-the-art methods. Then, we show how the learnable sphere cloud \mathbf{S} could be used to improve the volume rendering-based training process and finally describe the optimization pipeline for the sphere cloud itself.

3.1 Volume rendering

We assume the underlying implicit model f to represent the geometry of the surface, and for the transformation to exist that maps it to a surface density function $\sigma : \mathbb{R}^3 \rightarrow \mathbb{R}^+$, defined at each point \mathbf{x} in the volume.

In order to render the surface defined by σ via volumetric rendering, we first need to consider a ray $\mathbf{p}(t) = \mathbf{o} + t\mathbf{v}$, $t \geq 0$, emanated from the camera origin $\mathbf{o} \in \mathbb{R}^3$ in the direction $\mathbf{v} \in \mathbb{S}^2$, and the corresponding color $C(\mathbf{o}, \mathbf{v})$ of the pixel on the image plane of that camera. We also need to define a radiance field $c : \mathbb{R}^3 \times \mathbb{S}^2 \rightarrow \mathbb{R}^3$, which produces a view-dependent color at each point in the volume. The observed color $C(\mathbf{o}, \mathbf{v})$ can then be expressed as the following integral along the ray:

$$C(\mathbf{o}, \mathbf{v}) = \int_0^{+\infty} w(t)c(\mathbf{p}(t), \mathbf{v})dt, \quad (1)$$

where $w(t)$ is the probability of a ray terminating at $\mathbf{p}(t)$, which can be derived from the density σ :

$$w(t) = T(t)\sigma(t), \quad T(t) = \exp\left(-\int_0^t \sigma(s)ds\right). \quad (2)$$

In practice, the color integral is approximated by evaluating the density and radiance at a set of n sampled points $\mathcal{P} = \{\mathbf{p}_i = \mathbf{o} + t_i\mathbf{v}\}_{i=1}^n$ using the discretized version [20] of the equations above:

$$\hat{C}(\mathbf{o}, \mathbf{v}) = \sum_{i=1}^N T_i \alpha_i c_i, \quad T_i = \prod_{j=1}^{i-1} (1 - \alpha_j). \quad (3)$$

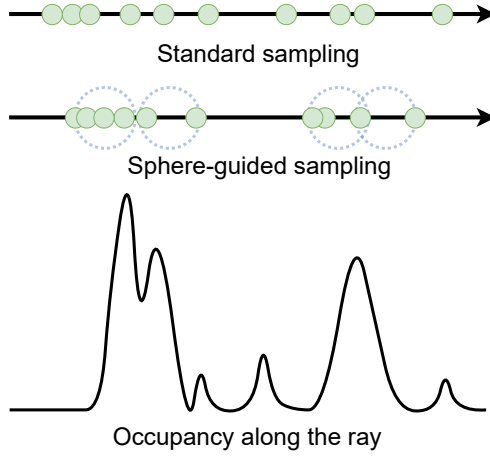


Figure 2: Our method works by filtering the samples along the ray which lie outside of the surface region, approximated by a guiding trainable sphere cloud. Such filtering reduces the noise in the optimization process, and allows the implicit function to converge to a better optima.

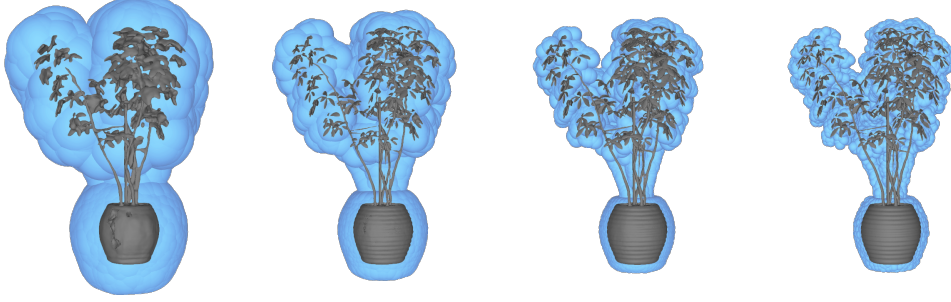


Figure 3: Visualization of the guiding sphere cloud alongside the implicit surface at different stages of the training. Initially, we assign all spheres a large radius due to high uncertainty of the implicit function’s gradients. We then gradually reduce it during training, which allows our representation to tightly follow the surface. At the same time, our proposed repulsion losses prevents the clumping of the spheres and encourages exploration, achieving proper surface coverage.

Here T_i denotes the accumulated transmittance and α_i — the opacity value at point \mathbf{p}_i , which can also be estimated from the density function via the following formula:

$$\alpha_i = 1 - \exp \left(- \int_{t_i}^{t_{i+1}} \sigma(t) dt \right). \quad (4)$$

3.2 Sphere-guided volume rendering

The sampling strategy for the points \mathcal{P} has a major impact on the resulting reconstructions since it directly affects the approximation quality of eq. 1. To improve it, some methods [22] employ the root-finding procedure to obtain the first intersection with the surface along the ray and sample more points near it. Other methods [4, 31, 38] are first estimating a dense set of proposals \mathcal{T} via importance or uncertainty sampling. Then, \mathcal{P} is obtained either via inverse transform sampling by evaluating the density σ at the proposals \mathcal{T} and normalizing it along the ray [4, 38], or in some cases by using an entire set of proposals [31].

To further improve the efficiency of both proposal sampling and root-finding procedures, we utilize a set of guiding spheres \mathbf{S} which surrounds the object’s surface. They allow us to ensure that the training samples \mathcal{P} are mainly generated from the areas of interest, making the implicit surface function converge to a better optimum, especially for the scenes with high-frequency details. We achieve that by applying both the root-finding and proposal sampling procedures only within the volume, defined by the sphere cloud \mathbf{S} . For the sampling of proposals \mathcal{T} , our method is described in the Algorithm 1, while the details of the modified root-finding approach can be found in the supplementary materials.

3.3 Sphere cloud optimization

At the beginning of training, we initialize the sphere cloud \mathbf{S} of size M with centers $\{\mathbf{c}_i\}_{i=1}^M$, uniformly distributed across the volume of the scene, and set the radii of the spheres to an initial value r_{\max} . The training then proceeds by alternating the updates of the sphere cloud and the implicit function. Importantly, we only update the sphere centers \mathbf{c}_i via an optimization-based process and rely on scheduling their radii to decrease from the initial value r_{\max} to the minimum r_{\min} via a fixed schedule. Also, in our approach, all spheres in the cloud are assigned the same radius value.

Algorithm 1: Sphere-guided sampling.

Input: ray $\mathbf{p}(t)$, spheres \mathbf{S} , #samples n

- 1 Initialize a set of intervals $\mathcal{I} = \emptyset$
 - 2 **for** $\mathbf{S}_i \in \mathbf{S}$ **do**
 - 3 Add sphere-ray intersection to \mathcal{I} :
 $\mathcal{I} := \mathcal{I} \cup \mathbf{S}_i \cap \mathbf{p}(t)$
 - 4 **end**
 - 5 Find a minimal set of intervals
 $\{[s_k, t_k]\} : \bigcup_k [\mathbf{p}(s_k), \mathbf{p}(t_k)] = \mathcal{I}$
 - 6 Initialize a set of points $\mathcal{T}_0 = \emptyset$
 - 7 **for** $k = 1 \dots K$ **do**
 - 8 Set $n_k := \lfloor n / (t_k - s_k) \rfloor$
 - 9 $\mathcal{T}_0 := \mathcal{T}_0 \cup \text{linspace}(s_k, t_k, n_k)$
 - 10 **end**
 - 11 Obtain \mathcal{T} using \mathcal{T}_0 and the sampling method of choice
 - 12 **return** \mathcal{T}
-

The main learning signal for the sphere centers comes from moving them towards the estimated surface \hat{S} , which is defined as an h -level set of the implicit function $f : \hat{S} = \{\mathbf{x} \in \mathbb{R}^3 \mid f(\mathbf{x}) = h\}$, where h depends on the type of the function (e.g., for SDF $h = 0$). This can be formulated as a following loss:

$$\mathcal{L}_{\text{surf}} = \sum_{i=1}^M \|f(\mathbf{c}_i) - h\|_2. \quad (5)$$

This objective ensures that the sphere centers lie in the proximity of the reconstructed surface, i.e., maximizes the precision. However, it does not guarantee that the point cloud covers an entire object’s surface. To address that, we design a repulsion term that prevents the neighboring spheres from clumping together and encourages exploration of the entire surface region:

$$\mathcal{L}_{\text{rep}} = \sum_{i=1}^M \sum_{j \in K(i)} r_n \frac{\mathbb{I}(\|\mathbf{c}_j - \mathbf{c}_i\|_2 < d)}{\|\mathbf{c}_j - \mathbf{c}_i\|_2}, \quad (6)$$

where $K(i)$ denotes the indices of the k -nearest spheres to \mathbf{S}_i , r_n is the current radius of the spheres, and d is a hyperparameter, which sets the maximum distance for the repulsion. Since the magnitude of this loss depends on the current radius of the spheres, the repulsion has more effect in the beginning of the training, encouraging better exploration of the scene volume.

Our final objective for optimization of the centers of the spheres is the following:

$$\mathcal{L} = \mathcal{L}_{\text{surf}} + \lambda \mathcal{L}_{\text{rep}}. \quad (7)$$

The radius scheduling in our method defines the exploration-exploitation trade-off and, in principle, could be picked separately for each scene. However, we found out that the following exponential schedule works well in most cases:

$$r_n = \max(r_{\text{max}} e^{-n\beta}, r_{\text{min}}). \quad (8)$$

Here, n denotes the training iteration, and β is a hyperparameter controlling the decay rate. We use the same β value across datasets and set it so that the radius reaches the minimum value of r_{min} in less than half of the training iterations.

To avoid problems with the sphere cloud convergence, we apply a resampling procedure for the empty spheres which get stuck without reaching the surface. This process is typically applied up to 8 times during training, depending on the total number of iterations. Similarly to [16], we sample K points inside each sphere at which we evaluate the implicit function and find the spheres which have no surface inside them. We then resample these spheres near the ones which contain a surface region. This regularization allows us to prune the noisy parts in the scene and increase the accuracy of the learned 3D representation. Lastly, to avoid choosing training rays that do not intersect the sphere cloud, we sample their endpoints uniformly across the object’s surface, similarly to [33]. For more details on the sphere resampling and sphere-guided ray sampling procedures, please refer to the supplementary materials.

4 Experiments

We conduct our main experiments using two popular 3D reconstruction benchmarks: DTU MVS [10] and Realistic Synthetic 360 [20] and evaluate our approach by combining it with four different methods for implicit surface reconstruction.

4.1 Base methods

Our approach acts as an addition to the 3D reconstruction systems that learn neural implicit surfaces through volume rendering. Therefore, we apply it to four representative systems to showcase its effectiveness and applicability. UNISURF [22] represents the geometry of the scene via an occupancy field that is learned through a combination of surface and volume rendering approaches. VolSDF [38] and NeuS [31] propose to train an SDF via volume rendering by transforming it into the volume density. NeuralWarp [4] builds upon VolSDF by using an additional loss term that directly enforces the photo consistency of the learned geometry by warping patches across different views. Our approach can be seamlessly incorporated into all these systems, and we provide additional implementation details in the supplementary materials.

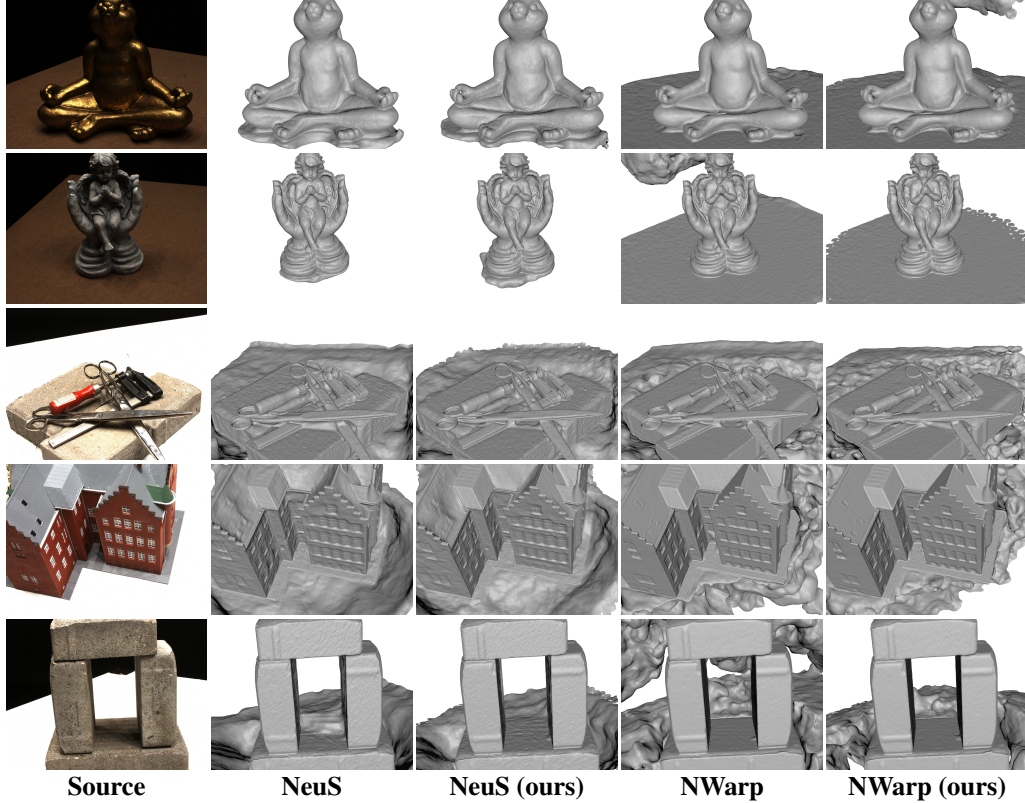


Figure 4: Qualitative results for our method on the DTU [10] dataset. We show that our approach is able to filter the noisy surfaces in the scenes, on average, better than the competitors, resulting in an increased quality of reconstructions without any segmentation-based post-processing of the obtained meshes. This is confirmed by a quantitative evaluation without masking, where NeuralWarp system with guiding spheres achieves an average Chamfer distance of 0.98 across all scenes, while the original method has an average distance of 1.05. For NeuS, the respective results are 0.94 with sphere guidance, and 1.04 without.

4.2 Training process

For each of the base models, we have used the official codebase, except for VolSDF, for which we use the code provided as part of the NeuralWarp method. Therefore, for the implementation aspects of the base methods, including the architectures and training details, we refer to the respective publications. We employ the same optimizer, scheduling, hyperparameters, number of iterations, and other technicalities as in the reference methods to train the implicit functions.

The sphere cloud optimization process is adapted for each system with regards to the implicit geometry type and the total number of iterations used for training. The sphere radius in the SDF-based methods decays exponentially from $r_{\max} = 0.4$ to $r_{\min} = 0.04$, while for UNISURF it ranges from $r_{\max} = 2.0$ to $r_{\min} = 0.1$. The repulsion penalty considers the $k = 10$ nearest spheres that intersect with each sphere in the cloud, i.e. $d = 2 * r_n$, and its weight is $\lambda = 0.1$ in UNISURF and $\lambda = 0.0001$ in the other methods. We found a number of 15,000 spheres to be sufficient for representing most scenes, which are scaled to fit in the bounding sphere of radius one, and address the exceptions in the limitations section. We employ Adam [13] optimizer with a learning rate of 10^{-4} for the optimization of the centers of the spheres in all experiments.

4.3 DTU evaluation

The DTU MVS dataset [10] contains 49 or 64 images with fixed camera positions and ground truth point clouds of 80 scenes acquired using a structured light scanner. We follow recent works [4, 22, 31, 38, 39] and perform evaluation on the subset of 15 diverse scenes selected by [39]. The authors

Table 1: We present a quantitative evaluation of our method on the DTU [10] dataset. We have combined our approach with four popular implicit surface reconstruction systems: UNISURF [22], NeuS [31], NeuralWarp [4], and VolSDF [38]. In this comparison, we follow the previous works by measuring the Chamfer distance (lower the better) between the ground truth point cloud and the reconstructions, pre-processed by removing the regions outside the object via ground-truth segmentation masks. The models in this comparison were trained *without* segmentation masks, unless stated otherwise. We highlight the better score between the original approach and our modification.

Method	Scene ID															Mean
	24	37	40	55	63	65	69	83	97	105	106	110	114	118	122	
UNISURF [22]	1.16	1.01	1.16	0.36	1.27	0.72	0.73	1.33	1.58	0.72	0.53	1.21	0.41	0.69	0.51	0.89
UNISURF (ours)	1.10	0.98	1.14	0.37	1.08	0.66	0.89	1.33	1.19	0.69	0.52	0.98	0.38	0.46	0.50	0.82
VolSDF* [38]	0.94	1.73	1.04	0.47	0.87	0.74	0.84	1.24	1.31	0.71	0.78	1.61	0.61	0.71	0.54	0.94
VolSDF* (ours)	0.91	1.05	0.65	0.42	0.86	0.69	0.72	1.20	1.14	0.64	0.66	1.16	0.43	0.54	0.51	0.77
NeuS [31]	0.93	1.06	0.81	0.38	1.02	0.60	0.58	1.43	1.15	0.78	0.57	1.15	0.35	0.45	0.46	0.78
NeuS (ours)	0.69	0.88	0.59	0.35	0.97	0.55	0.58	1.34	1.15	0.76	0.53	0.95	0.33	0.43	0.42	0.70
NeuS w/ masks	0.83	0.98	0.56	0.37	1.13	0.59	0.60	1.45	0.95	0.78	0.52	1.43	0.36	0.45	0.45	0.76
NeuS w/ m. (ours)	0.72	0.80	0.45	0.36	1.02	0.59	0.57	1.26	0.90	0.82	0.51	0.98	0.34	0.43	0.46	0.68
NeuralWarp [4]	0.49	0.71	0.38	0.38	0.79	0.81	0.82	1.20	1.06	0.68	0.66	0.74	0.41	0.63	0.51	0.68
NeuralWarp (ours)	0.49	0.77	0.37	0.40	0.81	0.87	0.72	1.19	1.07	0.66	0.64	0.70	0.37	0.58	0.48	0.68

* denotes unofficial implementation

Table 2: Quantitative results on the Realistic Synthetic 360 dataset [20]. We evaluate the Chamfer distance to compare the performance of different methods. We can see that base methods with our proposed modification achieve better performance than the original versions across almost all scenes. The gap is especially noticeable for the ficus and microphone (mic) scenes, where our method is able to help the base systems pick up and model thin details of the reconstructed object.

Method	Scene name								Mean
	Chair	Drums	Ficus	Hotdog	Lego	Mats	Mic	Ship	
NeuS [31]	0.45	3.18	1.59	0.66	0.81	0.47	5.82	1.80	1.85
NeuS (ours)	0.43	3.42	0.70	0.62	0.74	0.34	1.80	1.20	1.16
NeuS w/ masks	0.42	1.13	0.41	0.54	0.68	0.28	0.57	0.71	0.59
NeuS w/ m. (ours)	0.42	1.02	0.31	0.47	0.67	0.28	0.55	0.71	0.55
NeuralWarp [4]	0.46	3.94	0.87	1.59	1.00	1.10	0.89	1.49	1.42
NeuralWarp (ours)	0.42	2.56	0.55	1.50	0.85	0.99	0.73	1.36	1.12

also provide the corresponding segmentation masks for each of the chosen scenes, which are used in the “w/ masks” experiments.

For quantitative evaluation, we convert the trained implicit functions to triangle meshes using the Marching Cubes algorithm [15]. We then measure the Chamfer distances between the ground-truth point clouds and the extracted meshes using the standard evaluation procedure and report the scores in Table 1. These results are obtained without mask supervision during training, except for the “NeuS w/ masks” experiment. However, we follow other works in applying ground-truth masks for post-processing of the meshes before calculating the metrics. Specifically, we filter the mesh using the visual hull obtained from the multi-view segmentations dilated with a radius of 12. The visual hull is calculated as the intersection of the silhouette cones emitted from each of the training cameras. Notably, we use the same dilation radius for all of the compared methods, hence the reported metrics may differ from the ones presented in the original publications. As we can see from the results, our method improves three out of four base methods uniformly across most of the scenes.

To evaluate the denoising properties of our approach, we conduct both qualitative and quantitative evaluations of the raw meshes, without post-filtering with ground-truth masks. We observe (Figure 4) that our method produces significantly fewer artifacts outside the objects. We conduct an additional quantitative evaluation without mesh masking for two of the best-performing methods, NeuS and NeuralWarp, and find that in both cases our method improves the baseline results by a substantial margin (0.94 against 1.04 for NeuS, and 0.98 against 1.05 for NeuralWarp). This denoising property is especially useful for real-world applications, where segmentation masks may not be available.

4.4 Realistic Synthetic 360 evaluation

The Realistic Synthetic 360 dataset was introduced in [20] as a benchmark for the novel view synthesis task. Each of its 8 scenes features an object that is realistically rendered from 100 (training)

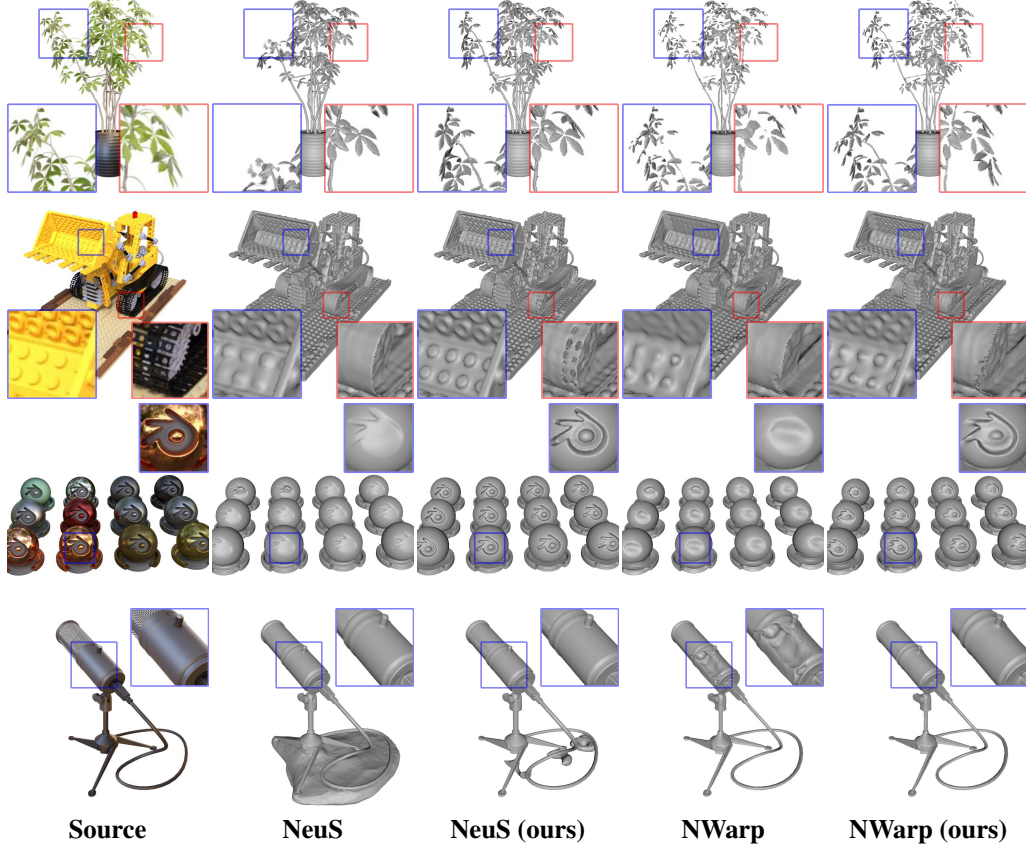


Figure 5: Qualitative results on the Realistic Synthetic 360 dataset [20]. We can see that the base methods achieve a better reconstruction fidelity, when sphere guiding is applied, especially high-frequency details are present on the objects’ surfaces (rows 2-3) or thin objects (row 1). We argue that to be the case due to the denser sampling of points near the surface, which allows our system to better learn the underlying geometry and consequently converge to a better local optima.

viewpoints, and paired with a ground truth mesh. Though this dataset was not originally intended for the 3D reconstruction task, it contains complex geometries with non-Lambertian materials, which represent a challenge for the classical 3D reconstruction systems. As some of the ground truth meshes contain internal surfaces that are not visible in any of the training views, we filter them by removing the non-visible parts. We perform a similar filtering step for the reconstructed meshes and compute the Chamfer distance between the cleaned meshes by sampling one million points on each surface. We report the distance computed at the original scale of the meshes multiplied by 10^2 in Table 2. We also report the qualitative results in Figure 5.

We can see that our method achieves almost uniform improvements across all the scenes for all of the compared methods. For some of the scenes, like ficus and materials, this improvement is especially noticeable. We hypothesize that this is the case because of the complex structure of the reconstructed surface. This complexity does not allow the standard methods to effectively estimate the location of the high-density regions, which hinders the optimization process, leading to both reduced quality of reconstructions and renders. For additional ablation experiments, as well as rendered results, please refer to the supplementary materials.

4.5 Ablation study

We have conducted an extensive ablation study to evaluate each component of our method. Both qualitative and quantitative results are presented in Figure 6. For the first experiment, we remove the repulsion loss \mathcal{L}_{rep} , and observe that it leads to spheres clumping together in the learned sphere cloud, not covering the entire object, which eventually produces poor reconstructions. For the next experiment, we remove the sphere-guided ray sampling, and instead select the rays uniformly across

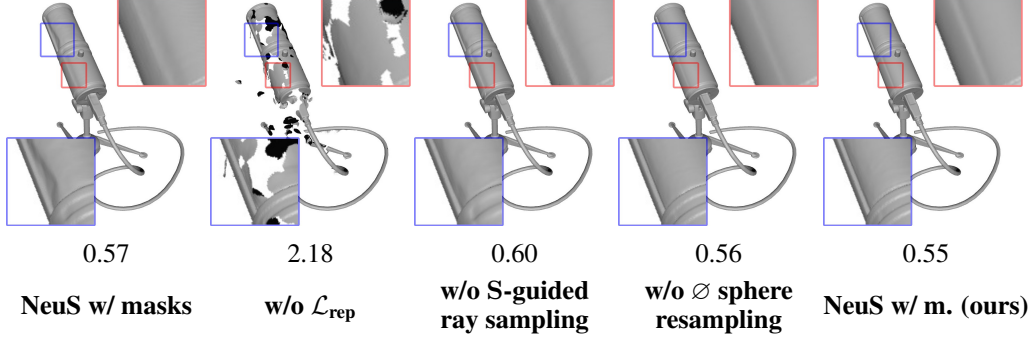


Figure 6: We present an ablation study, where we evaluate contributions of the individual parts of our method. We have used a NeuS system, trained with mask supervision, as a base model, and show both the resulting qualitative results, as well as obtained Chamfer distances for the shown scene. We can see that all parts of our method meaningfully contribute to the final results. For the detailed discussion, please refer to the ablation study section.

the image, as in the base methods. When the ray does not intersect any spheres, we employ a standard point sampling procedure of the base method (without sphere-guided sampling described in Algorithm 1). We observe that such modification leads to the decreased quality of reconstructions compared to both base and our full methods. Finally, we remove the estimation and resampling of empty spheres (i.e., the ones which do not contain any surface) from the pipeline, which also reduces the quality of the full method. For additional ablation experiments, please refer to the supplementary materials.

4.6 Limitations

Figure 7 depicts the main failure cases of the proposed approach. For some of the scenes, like drums in the first row, our method is lacking exploration and has erroneously pruned the objects like a chair or a drum cymbal as noise. We can see that while our proposed repulsion technique allows it to eventually discover thin parts of the scene like drum pedals and stand, missing in the base methods reconstruction, it fails to do so for the objects which are physically separated from the initially reconstructed objects. We also see that, despite effectively preventing the spheres from getting stuck in local optima, sometimes the sphere cloud fails to cover the entire surface which could result in holes appearing in the reconstruction (see the ship scene in the second row). Addressing these limitations remains an effort for future work.

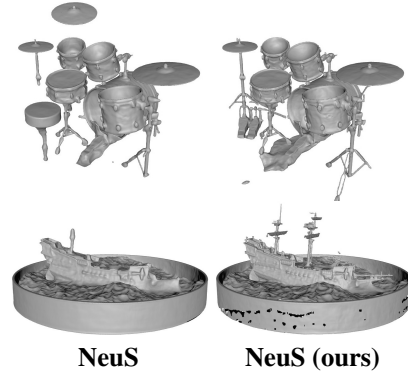


Figure 7: The limitations of our method. Our approach could erroneously treat some of the objects in the scene as noise and prune them. Also, despite the repulsion loss and resampling, in some cases the spheres could get stuck in local minimas and not cover an entire scene’s surface.

5 Conclusion

We have presented a method for improving volume rendering of implicit surface representations by restricting the modeled volume to the region of interest, defined by the set of trainable spheres. We have shown that focusing the optimization process on the estimated surface region leads to an increased quality of reconstructions obtained by the implicit functions. At the same time, our proposed sphere cloud optimization approach ensures that the guiding representation closely follows the estimated surface of the object and accurately represents it at each step of the training. We have conducted an extensive evaluation of our method, which includes combining it with four base systems for implicit function training, and found it to improve their performance across two benchmark datasets. Our method also shows clear gains for modeling the real-world scenes when applied without *any* additional supervision and post-filtering of the obtained reconstructions, which shows its suitability for in-the-wild applications.

Acknowledgments

We thank Taras Khakhulin for their comments and discussions. We also thank Francois Darmon for helping us reproduce the NeuralWarp results. The computational resources for this work were mainly provided by Samsung ML Platform.

References

- [1] Kara-Ali Aliev, Dmitry Ulyanov, and Victor S. Lempitsky. Neural point-based graphics. *ArXiv*, abs/1906.08240, 2020.
- [2] Michael Bleyer, Christoph Rhemann, and Carsten Rother. Patchmatch stereo - stereo matching with slanted support windows. In *BMVC*, 2011.
- [3] Neill D. F. Campbell, George Vogiatzis, Carlos Hernández, and Roberto Cipolla. Using multiple hypotheses to improve depth-maps for multi-view stereo. In *ECCV*, 2008.
- [4] Francois Darmon, B. Bascle, Jean-Clement Devaux, Pascal Monasse, and Mathieu Aubry. Improving neural implicit surfaces geometry with patch warping. *ArXiv*, abs/2112.09648, 2021.
- [5] Carlos Hernández Esteban and Francis J. M. Schmitt. Silhouette and stereo fusion for 3d object modeling. *Fourth International Conference on 3-D Digital Imaging and Modeling, 2003. 3DIM 2003. Proceedings.*, pages 46–53, 2003.
- [6] Yasutaka Furukawa and Carlos Hernández. Multi-view stereo: A tutorial. *Found. Trends Comput. Graph. Vis.*, 9:1–148, 2015.
- [7] Yasutaka Furukawa and Jean Ponce. Accurate, dense, and robust multiview stereopsis. *IEEE Transactions on Pattern Analysis and Machine Intelligence*, 32:1362–1376, 2010.
- [8] Amos Gropp, Lior Yariv, Niv Haim, Matan Atzmon, and Yaron Lipman. Implicit geometric regularization for learning shapes. In *ICML*, 2020.
- [9] Po-Han Huang, Kevin Matzen, Johannes Kopf, Narendra Ahuja, and Jia-Bin Huang. Deepmvs: Learning multi-view stereopsis. *2018 IEEE/CVF Conference on Computer Vision and Pattern Recognition*, pages 2821–2830, 2018.
- [10] Rasmus Ramsbol Jensen, A. Dahl, George Vogiatzis, Engil Tola, and Henrik Aanæs. Large scale multi-view stereopsis evaluation. *2014 IEEE Conference on Computer Vision and Pattern Recognition*, pages 406–413, 2014.
- [11] James T. Kajiya and Brian Von Herzen. Ray tracing volume densities. *Proceedings of the 11th annual conference on Computer graphics and interactive techniques*, 1984.
- [12] Petr Kellnhofer, Lars Jebe, Andrew Jones, Ryan P. Spicer, Kari Pulli, and Gordon Wetzstein. Neural lumigraph rendering. *2021 IEEE/CVF Conference on Computer Vision and Pattern Recognition (CVPR)*, pages 4285–4295, 2021.
- [13] Diederik P. Kingma and Jimmy Ba. Adam: A method for stochastic optimization. *CoRR*, abs/1412.6980, 2015.
- [14] Christoph Lassner and Michael Zollhöfer. Pulsar: Efficient sphere-based neural rendering. *2021 IEEE/CVF Conference on Computer Vision and Pattern Recognition (CVPR)*, pages 1440–1449, 2021.
- [15] Thomas Lewiner, Hélio Lopes, Antônio Wilson Vieira, and Geovan Tavares. Efficient implementation of marching cubes’ cases with topological guarantees. *Journal of Graphics Tools*, 8(2):1–15, 2003.
- [16] Lingjie Liu, Jiatao Gu, Kyaw Zaw Lin, Tat-Seng Chua, and Christian Theobalt. Neural sparse voxel fields. *Advances in Neural Information Processing Systems*, 33:15651–15663, 2020.
- [17] Stephen Lombardi, Tomas Simon, Jason M. Saragih, Gabriel Schwartz, Andreas M. Lehrmann, and Yaser Sheikh. Neural volumes. *ACM Transactions on Graphics (TOG)*, 38:1 – 14, 2019.
- [18] Stephen Lombardi, Tomas Simon, Gabriel Schwartz, Michael Zollhoefer, Yaser Sheikh, and Jason M. Saragih. Mixture of volumetric primitives for efficient neural rendering. *ACM Transactions on Graphics (TOG)*, 40:1 – 13, 2021.

- [19] Keyang Luo, Tao Guan, Lili Ju, Yuesong Wang, Zhuo Chen, and Yawei Luo. Attention-aware multi-view stereo. In *Proceedings of the IEEE/CVF Conference on Computer Vision and Pattern Recognition*, pages 1590–1599, 2020.
- [20] Ben Mildenhall, Pratul P. Srinivasan, Matthew Tancik, Jonathan T. Barron, Ravi Ramamoorthi, and Ren Ng. Nerf: Representing scenes as neural radiance fields for view synthesis. In *ECCV*, 2020.
- [21] Thomas Müller, Alex Evans, Christoph Schied, and Alexander Keller. Instant neural graphics primitives with a multiresolution hash encoding. *ArXiv*, abs/2201.05989, 2022.
- [22] Michael Oechsle, Songyou Peng, and Andreas Geiger. Unisurf: Unifying neural implicit surfaces and radiance fields for multi-view reconstruction. *2021 IEEE/CVF International Conference on Computer Vision (ICCV)*, pages 5569–5579, 2021.
- [23] Ruslan Rakhimov, Andrei Ardelean, Victor S. Lempitsky, and Evgeny Burnaev. Npbg++: Accelerating neural point-based graphics. *ArXiv*, abs/2203.13318, 2022.
- [24] Gernot Riegler and Vladlen Koltun. Stable view synthesis. In *Proceedings of the IEEE/CVF Conference on Computer Vision and Pattern Recognition*, pages 12216–12225, 2021.
- [25] Darius Rückert, Linus Franke, and Marc Stamminger. Adop: Approximate differentiable one-pixel point rendering. *ArXiv*, abs/2110.06635, 2021.
- [26] Johannes L. Schönberger, Enliang Zheng, Jan-Michael Frahm, and Marc Pollefeys. Pixelwise view selection for unstructured multi-view stereo. In *ECCV*, 2016.
- [27] Christoph Strecha, Wolfgang von Hansen, Luc Van Gool, P. Fua, and Ulrich Thoennessen. On benchmarking camera calibration and multi-view stereo for high resolution imagery. *2008 IEEE Conference on Computer Vision and Pattern Recognition*, pages 1–8, 2008.
- [28] Cheng Sun, Min Sun, and Hwann-Tzong Chen. Direct voxel grid optimization: Super-fast convergence for radiance fields reconstruction. *ArXiv*, abs/2111.11215, 2021.
- [29] Justus Thies, Michael Zollhöfer, and Matthias Nießner. Deferred neural rendering: Image synthesis using neural textures. *ACM Transactions on Graphics (TOG)*, 38(4):1–12, 2019.
- [30] Fangjinhua Wang, Silvano Galliani, Christoph Vogel, Pablo Speciale, and Marc Pollefeys. Patchmatchnet: Learned multi-view patchmatch stereo. In *Proceedings of the IEEE/CVF Conference on Computer Vision and Pattern Recognition*, pages 14194–14203, 2021.
- [31] Peng Wang, Lingjie Liu, Yuan Liu, Christian Theobalt, Taku Komura, and Wenping Wang. Neus: Learning neural implicit surfaces by volume rendering for multi-view reconstruction. *ArXiv*, abs/2106.10689, 2021.
- [32] Xiang Wang, Chen Wang, Bing Liu, Xiaoqing Zhou, Liang Zhang, Jin Zheng, and Xiao Bai. Multi-view stereo in the deep learning era: A comprehensive review. *Displays*, 70:102102, 2021.
- [33] Yifan Wang, Shihao Wu, A. Cengiz Öztireli, and Olga Sorkine-Hornung. Iso-points: Optimizing neural implicit surfaces with hybrid representations. *2021 IEEE/CVF Conference on Computer Vision and Pattern Recognition (CVPR)*, pages 374–383, 2021.
- [34] Olivia Wiles, Georgia Gkioxari, Richard Szeliski, and Justin Johnson. Synsin: End-to-end view synthesis from a single image. *2020 IEEE/CVF Conference on Computer Vision and Pattern Recognition (CVPR)*, pages 7465–7475, 2020.
- [35] Qiangeng Xu, Zexiang Xu, Julien Philip, Sai Bi, Zhixin Shu, Kalyan Sunkavalli, and Ulrich Neumann. Point-nerf: Point-based neural radiance fields. *ArXiv*, abs/2201.08845, 2022.
- [36] Jiayu Yang, Wei Mao, Jose M Alvarez, and Miaomiao Liu. Cost volume pyramid based depth inference for multi-view stereo. In *Proceedings of the IEEE/CVF Conference on Computer Vision and Pattern Recognition*, pages 4877–4886, 2020.
- [37] Yao Yao, Zixin Luo, Shiwei Li, Tian Fang, and Long Quan. Mvsnet: Depth inference for unstructured multi-view stereo. In *Proceedings of the European Conference on Computer Vision (ECCV)*, pages 767–783, 2018.
- [38] Lior Yariv, Jiatao Gu, Yoni Kasten, and Yaron Lipman. Volume rendering of neural implicit surfaces. *ArXiv*, abs/2106.12052, 2021.

- [39] Lior Yariv, Yoni Kasten, Dror Moran, Meirav Galun, Matan Atzmon, Ronen Basri, and Yaron Lipman. Multiview neural surface reconstruction by disentangling geometry and appearance. *arXiv: Computer Vision and Pattern Recognition*, 2020.
- [40] Alex Yu, Sara Fridovich-Keil, Matthew Tancik, Qinhong Chen, Benjamin Recht, and Angjoo Kanazawa. Plenoxels: Radiance fields without neural networks. *ArXiv*, abs/2112.05131, 2021.
- [41] Alex Yu, Ruilong Li, Matthew Tancik, Hao Li, Ren Ng, and Angjoo Kanazawa. Plenotrees for real-time rendering of neural radiance fields. In *Proceedings of the IEEE/CVF International Conference on Computer Vision*, pages 5752–5761, 2021.
- [42] Jingyang Zhang, Yao Yao, Shiwei Li, Zixin Luo, and Tian Fang. Visibility-aware multi-view stereo network. *ArXiv*, abs/2008.07928, 2020.

A Implementation details

Sphere resampling. We employ sphere resampling to ensure all the primitives model the area of interest. To identify the spheres that fail to reach the surface due to local minimum regions of the implicit geometry field, we uniformly sample $K = 1000$ points in each sphere and evaluate the implicit function. Then, we mark the spheres that contain points either with all values lower, or all values higher than the surface level. Each marked sphere is replaced as follows: we randomly pick a sphere that is not marked and center a Gaussian distribution with a standard deviation of $\sigma = 2 * r_{min}$ around its origin, we sample the new origin of the sphere from this distribution, finally, we reinitialize the optimizer state for the considered primitive. A similar resampling strategy is applied periodically after every 1000 iterations for the spheres that are pushed by the repulsion outside of the scene bounds.

We found the resampling of empty spheres to bring the most benefits to UNISURF [22] model which uses an occupancy field for the implicit surface. This representation is more susceptible to local minimums than the SDF which has an additional Eikonal regularization [8]. Also, the number of spheres that require resampling for NeuralWarp [4] / VolSDF [38] is around 10 times higher in the initial steps than for NeuS [31]. We believe this is because the former imposes the Eikonal penalty only on two points on each ray, while the latter constrains the gradients of all points sampled along the ray.

Sphere-guided ray sampling. Compared to base methods, the sphere-guided models have the relevant areas of the volume explicitly defined. We can exploit the sphere bounds into sampling more informative rays during training as follows: we randomly sample a point inside each sphere and project the points to the training views. We exclude the points that project outside of the image bounds and randomly sample from the remaining points a batch of corresponding camera rays which are used for a training step.

Sphere-guided sampling. The proposed approach can be applied to the considered 3D reconstruction methods without altering their formulation and training process. However, the introduced sphere-guided volume rendering enhances the sampling procedures of the base methods as described in **Algorithm 1**, which imposes the following modifications:

- UNISURF [22] - the root-finding procedure is adjusted by only searching for the surface within the volume covered by the spheres. More precisely, we sample points uniformly inside the intervals (as found at step 5 of the algorithm) to find the first sign change. We then apply the secant method on this segment as in the original method. Reducing the search to the area around the surface enables the algorithm to better estimate the ray-surface intersection. The rest of the sampling procedure follows the original model.
- NeuS [31] - the points sampled within the ray-sphere intersections are used to compute a coarse probability estimation along the ray. If the ray intersects multiple surfaces, the set computed at step 5 of the algorithm can have more than one interval. As the region between two such intervals is outside the sphere cloud, we do not want to include it in the importance sampling. Therefore, we set the probabilities of these regions to zero which ensures that the added points through importance sampling will belong to the set of intervals. Similarly, we set the weights of the midpoints used in color computation that fall outside the sphere bounds to zero. In the experiments that do not have segmentation masks as input, NeuS samples a set of points outside the bounds of the scene for background modeling; we do not interfere with these samples.
- VolSDF [38] / NeuralWarp [4] - We perform similar modifications as in NeuS model. We set the uncertainty estimation of the ray segments between intervals to zero, so that the points added during the upsampling stage are contained within the intersections of the ray with the sphere cloud. Additionally, we consider the estimated opacity of the previously mentioned segments as zero before performing inverse transform sampling, to ensure that the final set of points lies within the intervals computed at step 5 of the algorithm. We do not interfere with the points sampled in the base method for background modeling outside the scene bounds.

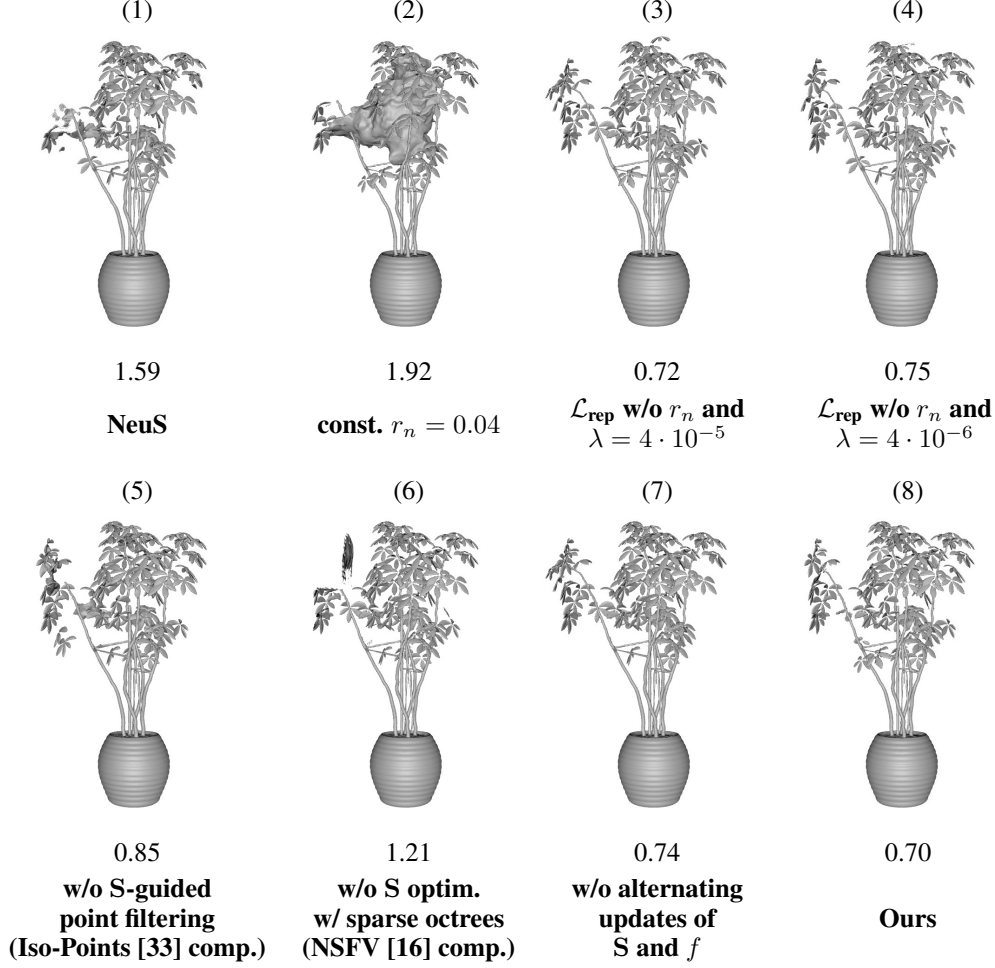


Figure 8: Extended ablation study of our approach. For each reconstruction, Chamfer distances are reported under the rendered meshes. We explore the effect of the following features of our method: (2) the scheduling of radius (by setting r_n to a constant minimum value); (3-4) scheduling of the repulsion loss, carried out by fixing it to either maximum (3) or minimum (4) values; (5) sphere-guided point filtering (without it our method becomes similar to the Iso-Points [33] approach); (6) gradient-based optimization of the sphere cloud, which we ablate via an alternative heuristic optimization strategy using sparse voxel octrees, proposed in Neural Sparse Voxel Fields (NSFV) [16]; (7) finally, we remove alternating updates of \mathbf{S} and f and instead update them via a schedule, 5000 iterations each. All of these modifications meaningfully contribute to the final quality of our method, shown in (8), while most of them also improve the quality of the base method, shown in (1).

B Additional results

B.1 Extended ablation study.

We provide an extended ablation study with the results presented in Figure 8.

- We show that our proposed scheduling of the repulsion loss, as well as the radius of the spheres, all meaningfully contribute to the final quality of the results (Subfigures 2-4).
- We conduct a comparison with an upgraded version of the Iso-Points [33] method, see Subfigure 5. We keep our proposed optimization scheme for the sphere cloud but remove the sphere-based sampling of points along the ray. We observe that such changes noticeably decrease the quality of reconstructions compared to our final method.

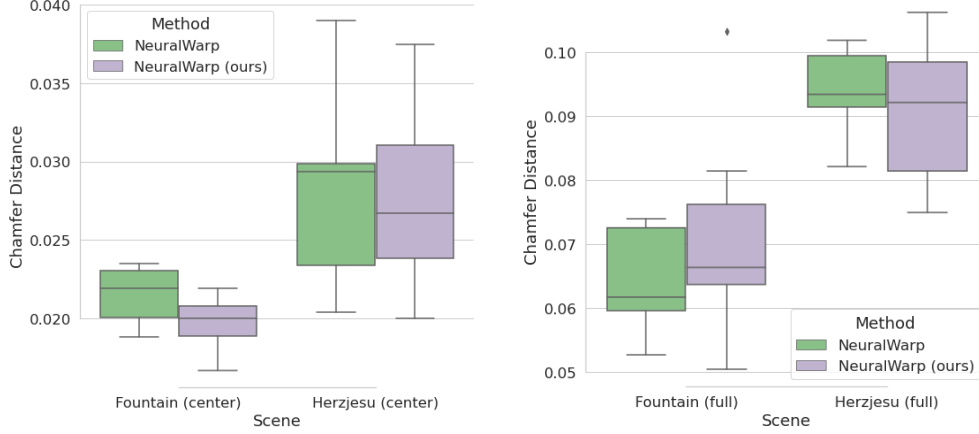


Figure 9: Quantitative results for the two scenes of the EPFL [27] dataset. Following NeuralWarp [4], we measure the performance of our method on two scenes in two scenarios: the full scene and its center crop. To account for the stochasticity of the base method, we train the reconstruction of each scene ten times with different random seeds. The results are reported as box plots, where the middle line denotes the median, the box boundaries denote 25th and 75-th percentiles, and whiskers denote the minimum and maximum values. We can see that, on average, our approach improves NeuralWarp for the center parts of the scenes (left plot) while having mixed results for the full scenes (right plot).

- We evaluate the effect of our gradient-based sphere cloud optimization scheme has on the learned reconstructions. To do that, we replace our sphere cloud with a sparse voxel octree data structure and use its optimization method proposed in Neural Sparse Voxel Fields [16] paper. We initialize our sparse voxel grid with 512 voxels, and use the same scheduling for pruning and subdivision, as in the original NSFV approach, multiplied by a factor of two (since we use two times more iterations for training). For pruning of voxels, we utilize the same sphere resampling criteria, as in our method, but relaxed it to allow the spheres within an ϵ distance to the surface to be not pruned. We did experiments for $\epsilon = 0.0, 0.1, 0.01$, and 10^{-4} , and found the experiment with $\epsilon = 0.1$ to achieve the best performance, while the experiment with $\epsilon = 0.0$ failed to converge to a non-empty surface. The results of the experiment with $\epsilon = 0.1$ is reported in Figure 8 (Subfigure 6). We can see that our gradient-based optimization method of the sphere cloud outperforms the training method for the sparse voxel octrees, proposed in [16].
- Lastly, we evaluate the effect alternating gradient descent optimization strategy has on the final result. To do that, we tried changing the optimization strategy for the sphere cloud \mathbf{S} and an implicit function f by alternating every 5000 iterations instead of one (see Subfigure 7). The resulting reconstruction lacks some of the details, presented in our final method, which proves the exploration capabilities of our proposed alternating optimization process.

B.2 Computational resources.

We used a private Samsung ML Platform cluster to carry out most of the experiments. We trained all models using NVIDIA P40 GPUs, with each experiment running on a single GPU. All our experiments took approximately 2,000 GPU-days to carry out, which includes the model design and search for optimal hyperparameters.

B.3 Extended qualitative and quantitative comparison.

We also include results for a number of experiments, not present in the main part of the paper.

EPFL dataset experiments. We evaluate the performance of our model, compared to the NeuralWarp [4] method, on EPFL [27] benchmark. The quantitative results are presented in Figure 9, and qualitative in Figure 11. To alleviate the effect that stochasticity in the NeuralWarp method has on the resulting reconstructions, we have conducted these experiments by training all models with ten

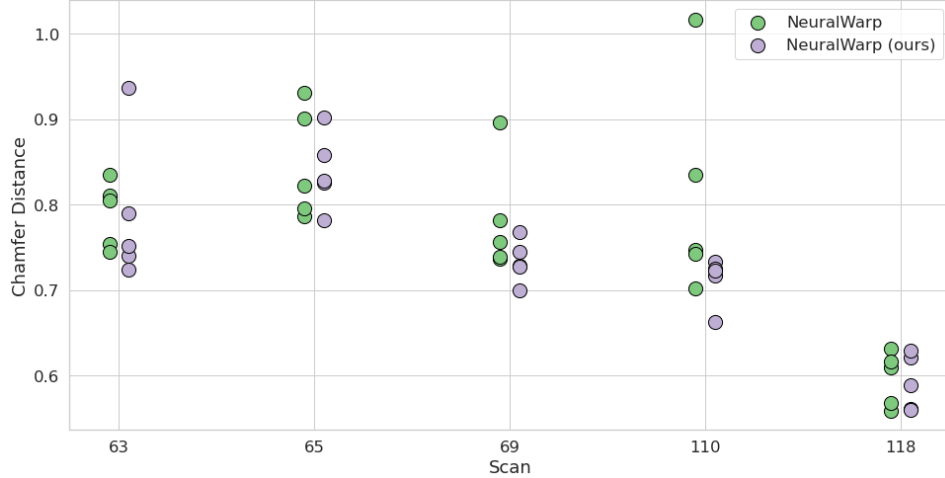


Figure 10: Quantitative results for the subset of five scenes of the DTU [10] dataset. We separately train each method for each scene five times with different starting random seeds. The results for our approach are reported in green, while for the base method they are in purple. The x -axis represents the scene ID, and the y -axis shows the obtained Chamfer distances. This comparison utilizes a masked Chamfer distance, following the same setting as in Table 1 in the experiments section. Our approach achieves a noticeably reduced variance of the results compared to the base system, and outperforms it on average, obtaining mean Chamfer distance of 0.73, averaged across five seeds and five scans, against the NeuralWarp’s 0.76. We also have better worst- and best-case performance, with our method having mean best-case metrics of 0.69 against NeuralWarp’s 0.71 and mean worst-case of 0.79 against 0.86.

different random seeds and reported the results as box plots. We can see that for the center part of the scene our method, on average, performs better than NeuralWarp, while for the full scene our method increases the stochasticity for some of the scenes. We argue that is the case due to not using any specific initialization for the EPFL scenes, which leads to a large chunk of spheres being initialized far from the actual surface and not being able to converge there. Scene-specific initialization or initialization using a point cloud extracted from Structure-from-Motion methods could lead to better results. Exploring these options remains our future work.

DTU dataset experiments. We show additional quantitative (Figure 10) and qualitative (Figures 12-15) evaluation of our method on the DTU [10] dataset. In Figure 10, we investigate more in-depth the comparative performance between our method and NeuralWarp. To this end, we randomly picked five scenes and trained four models with different random seeds. We add these data points to the ones reported in the main paper and present them in this figure. We conclude that, on average, our method performs better than raw NeuralWarp, when the stochasticity of the base method is accounted for. Our method on average achieves a mean Chamfer distance of 0.73 against the NeuralWarp’s 0.76. We also show additional qualitative results for six more scenes of DTU dataset in Figures 12-15.

Realistic Synthetic 360 dataset [20] experiments. Lastly, we present both results for the remaining scenes of the Realistic Synthetic 360 dataset [20] in Figures 16-17, as well as renders in Figures 18-19. We observe that our method not only achieves superior quality of reconstruction, but also renders. The views we used for rendering are sampled from the test set and are unseen during training.

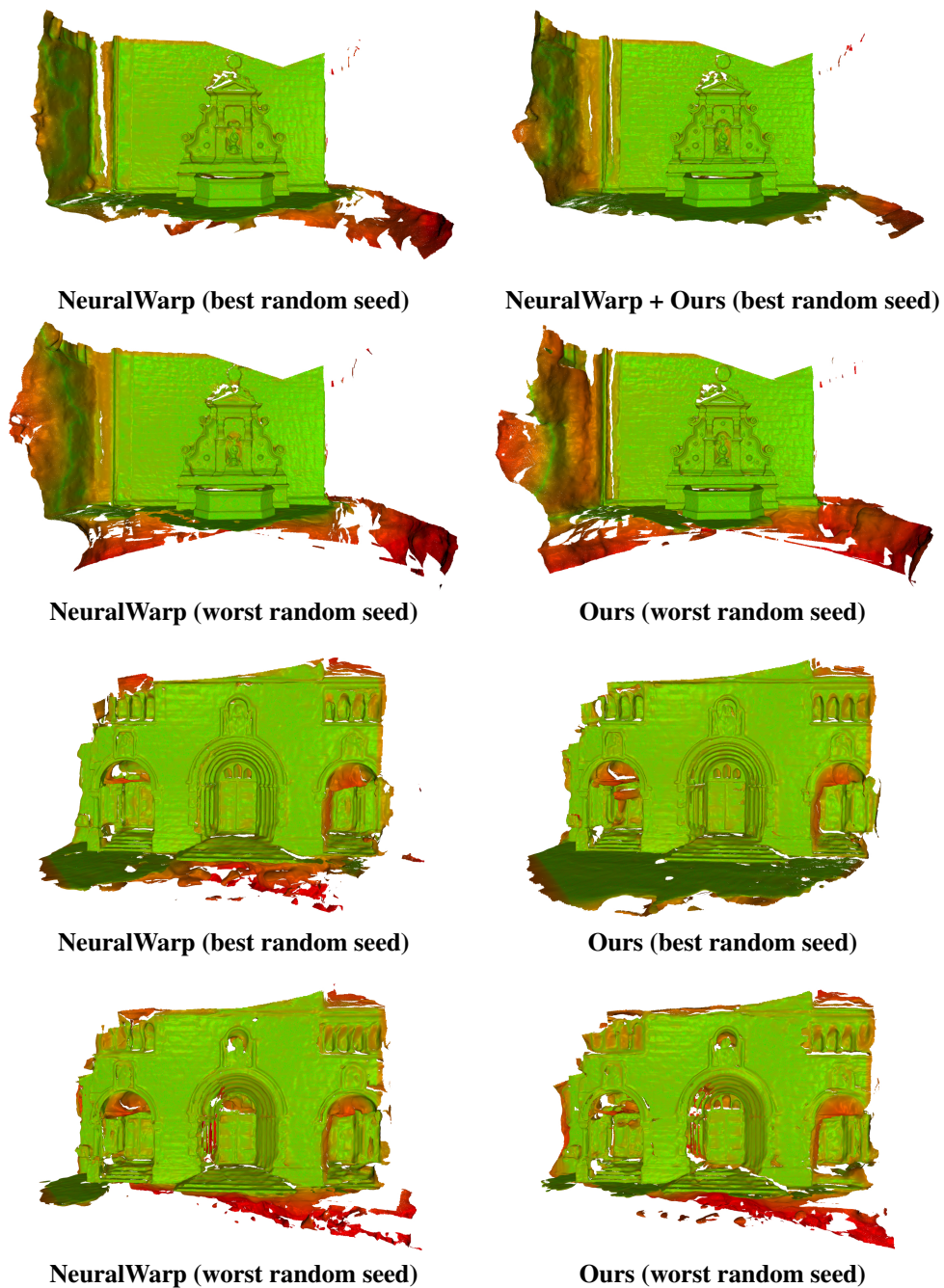


Figure 11: Qualitative results for two scenes of the EPFL [27] dataset. We evaluate our approach by applying it to the NeuralWarp system. The results are presented for the best and the worst checkpoints (according to the Chamfer distance), obtained from ten random initializations. We can see that our method outperforms the base system in the central regions both in the best and worst case initializations, while outperforming the base method on the full scenes in the best case. Digital zoom-in recommended.

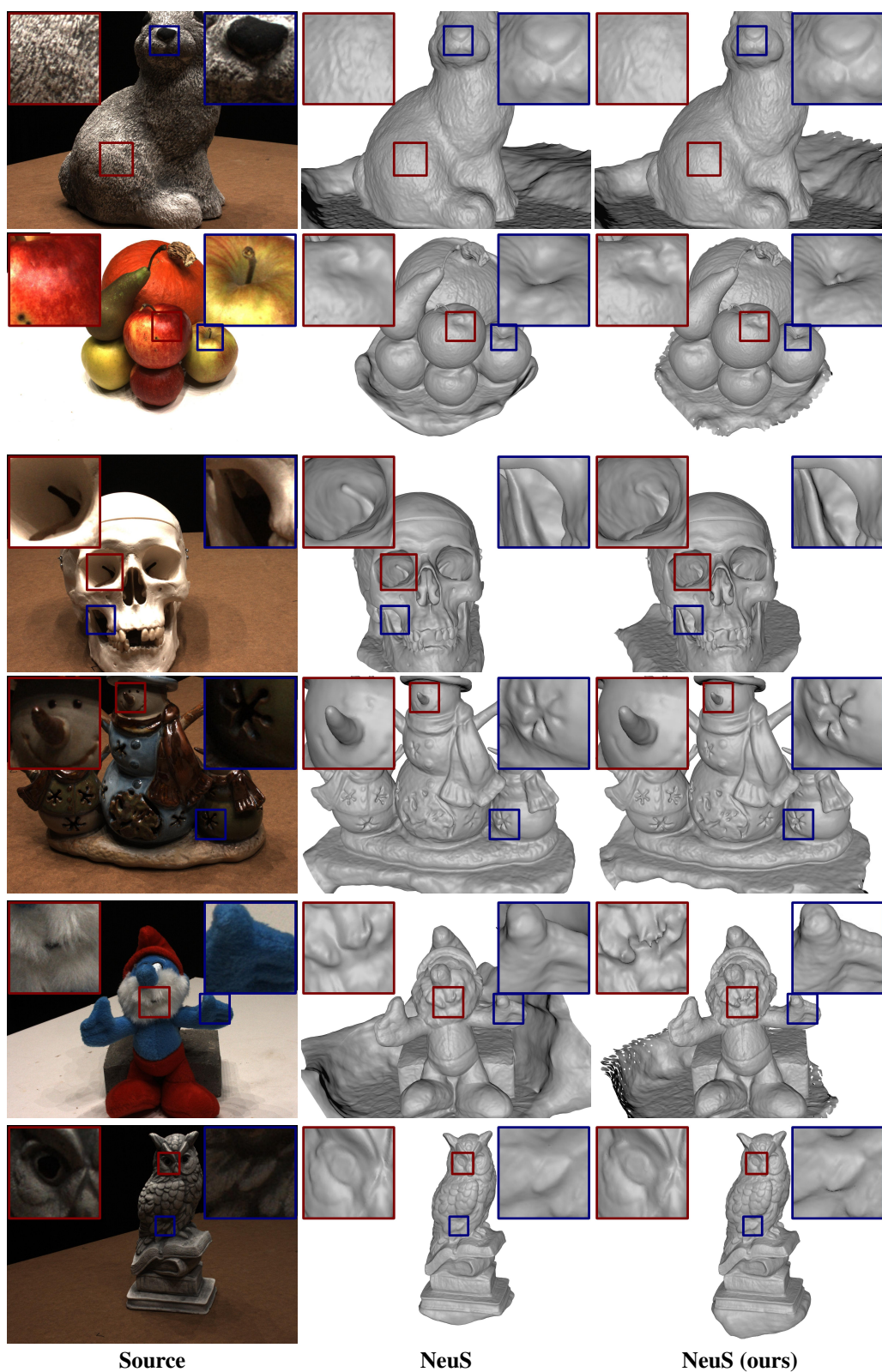


Figure 12: Additional qualitative results on the DTU [10] dataset for NeuS [31] method.

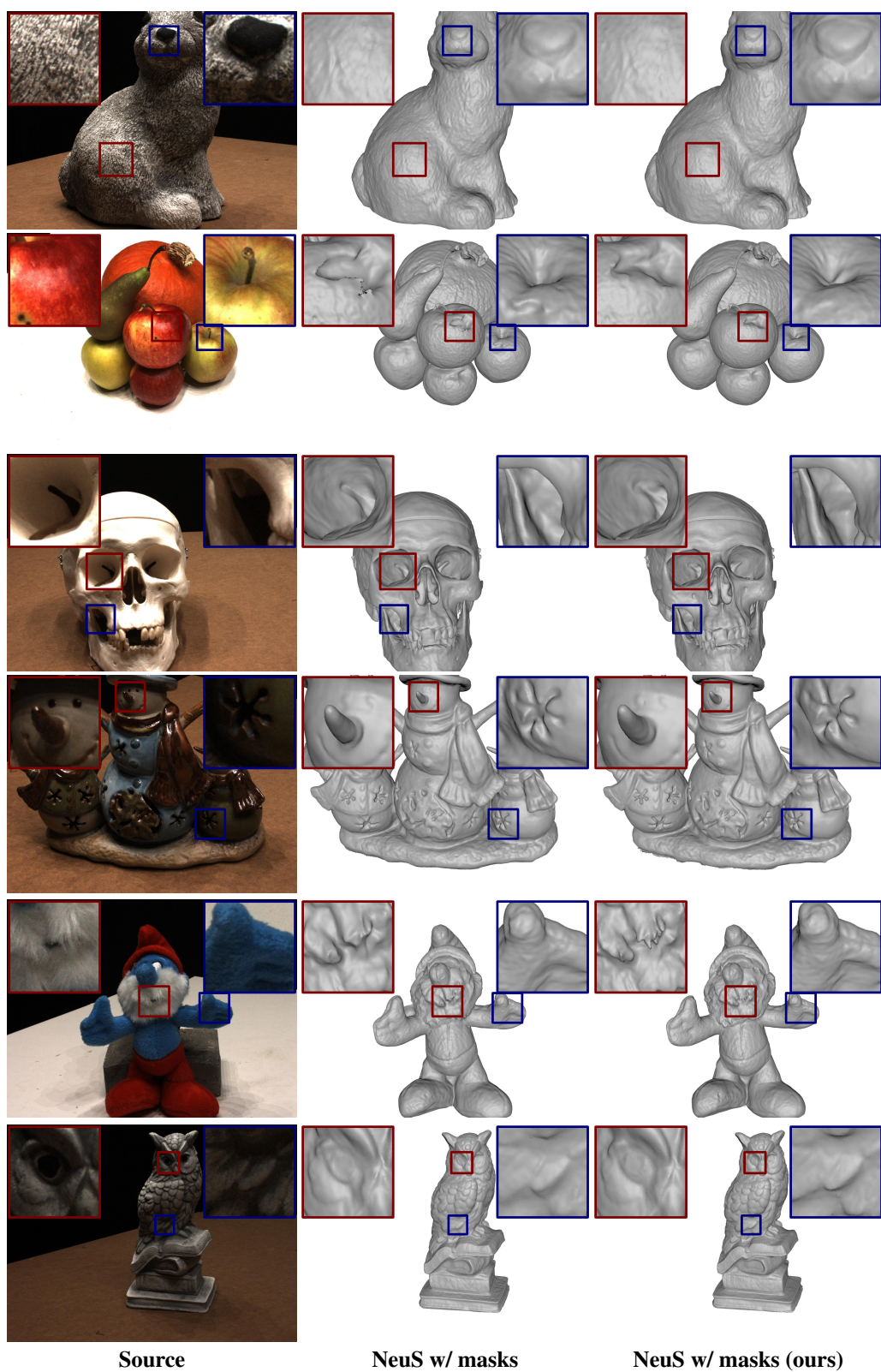


Figure 13: Additional qualitative results on the DTU [10] dataset for NeuS [31] method trained with masks supervision.

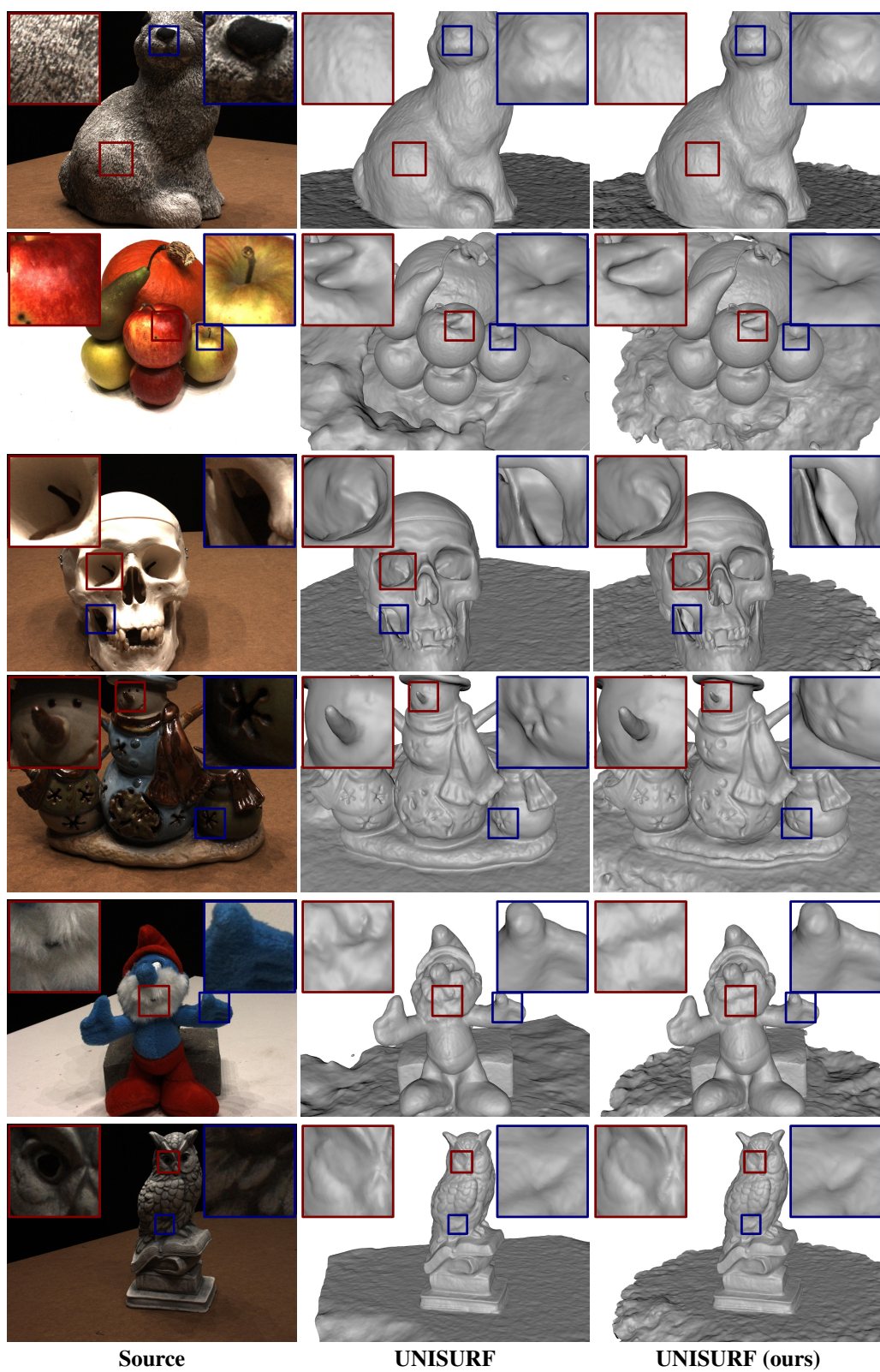


Figure 14: Additional qualitative results on the DTU [10] dataset for UNISURF [22] method.

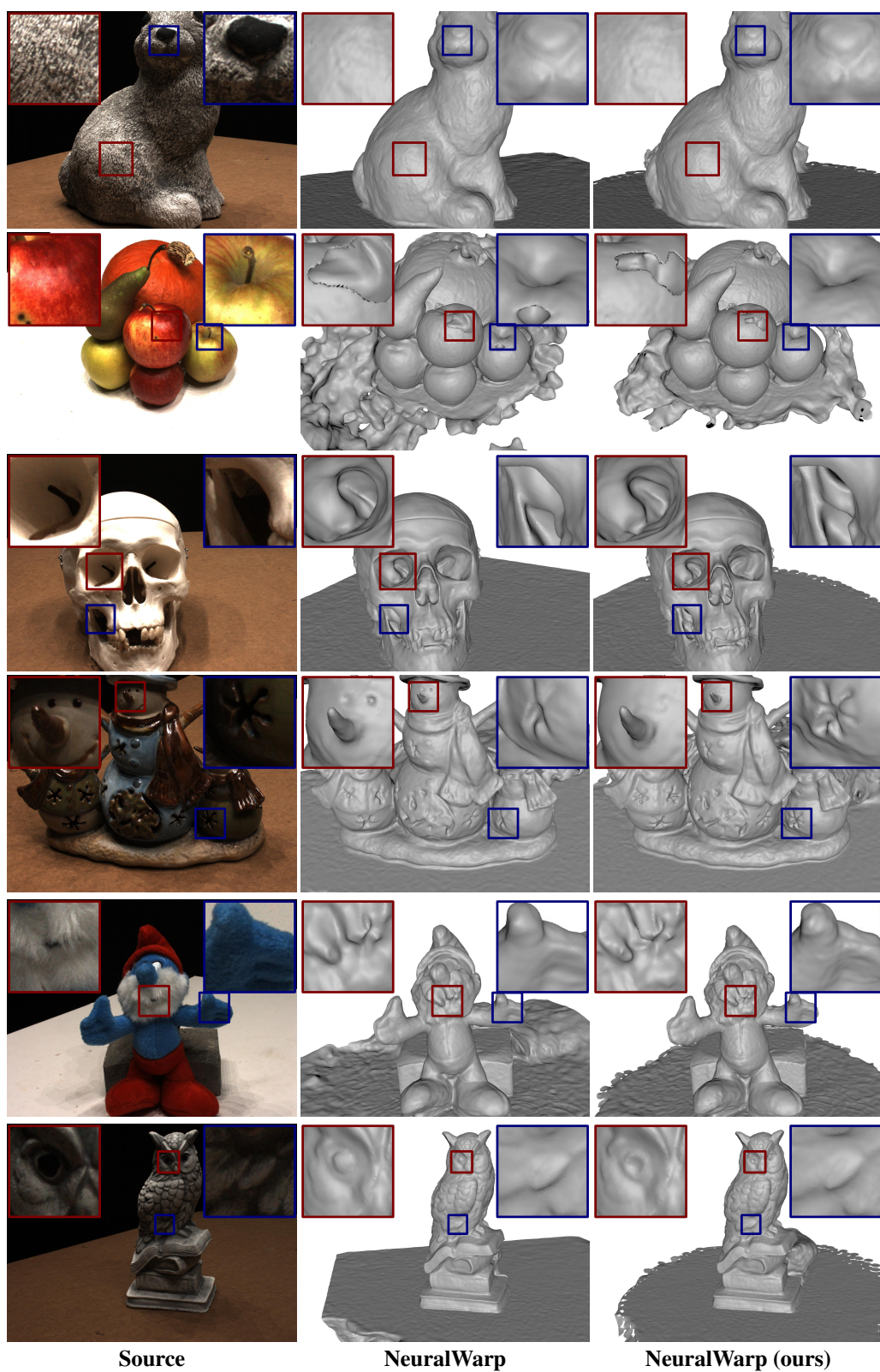


Figure 15: Additional qualitative results on the DTU [10] dataset for NeuralWarp [4] method.

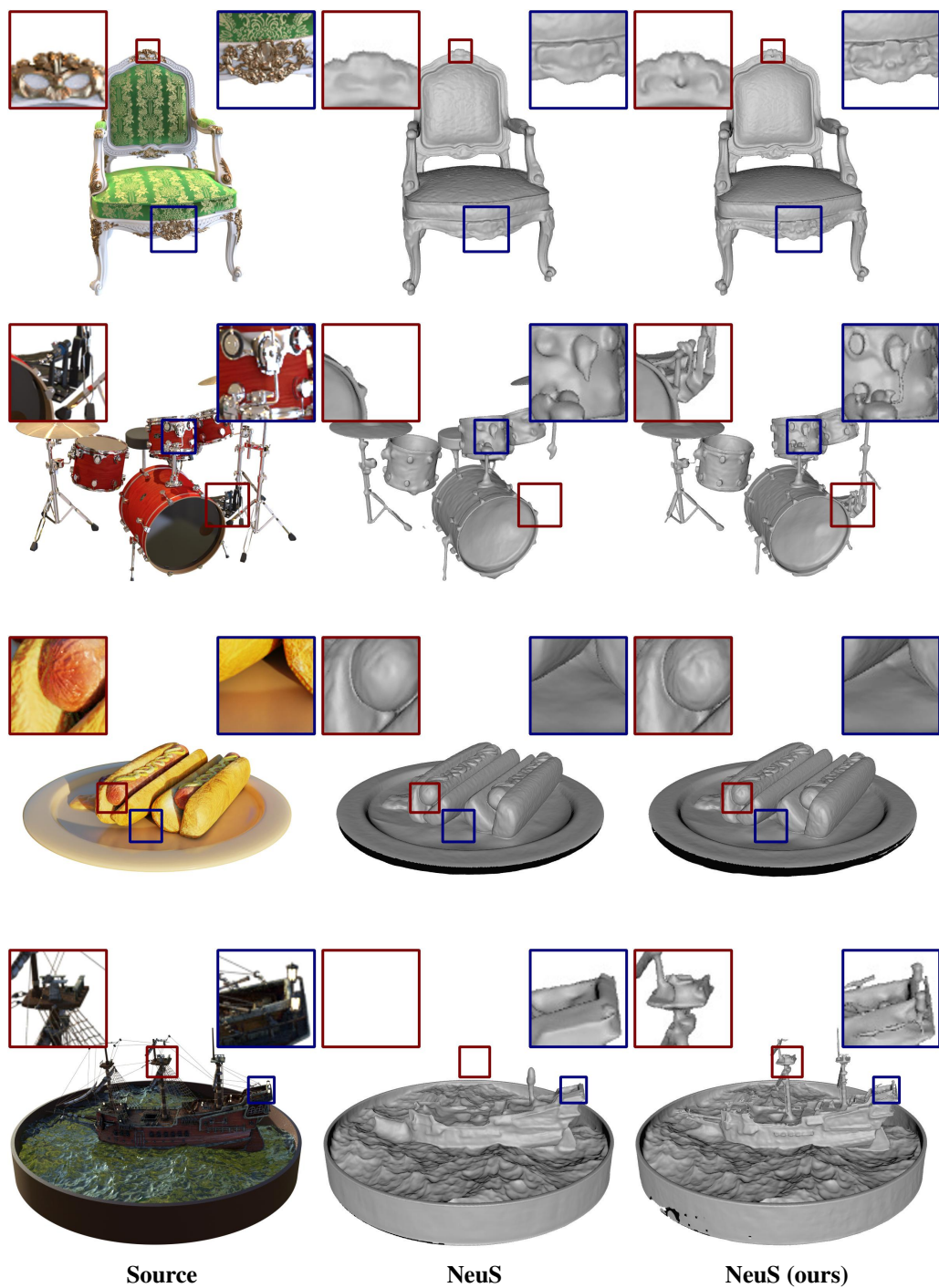


Figure 16: Additional qualitative results on the Realistic Synthetic 360 dataset [20] for NeuS [31] method.

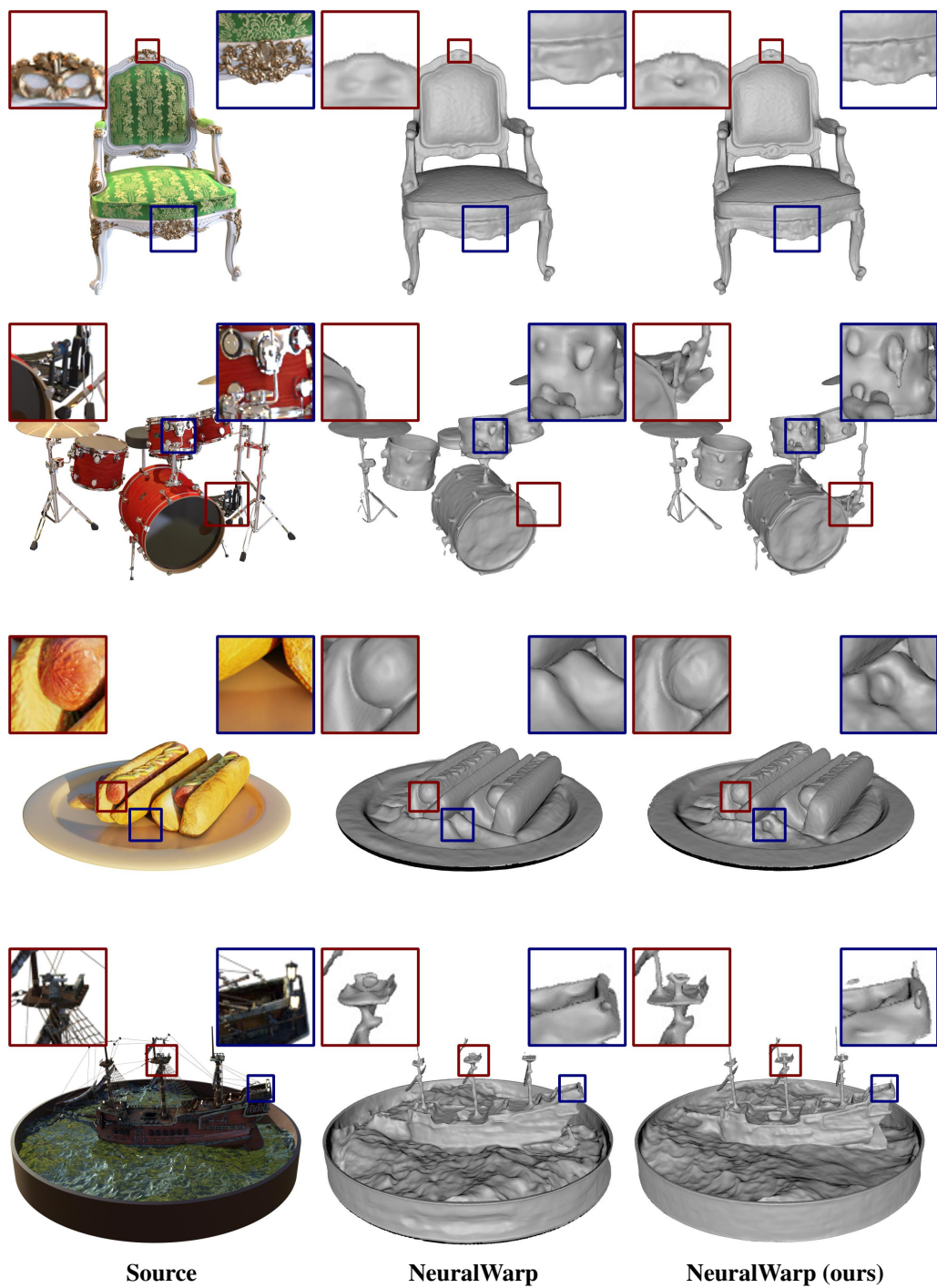


Figure 17: Additional qualitative results on the Realistic Synthetic 360 dataset [20] for NeuralWarp [4] method.

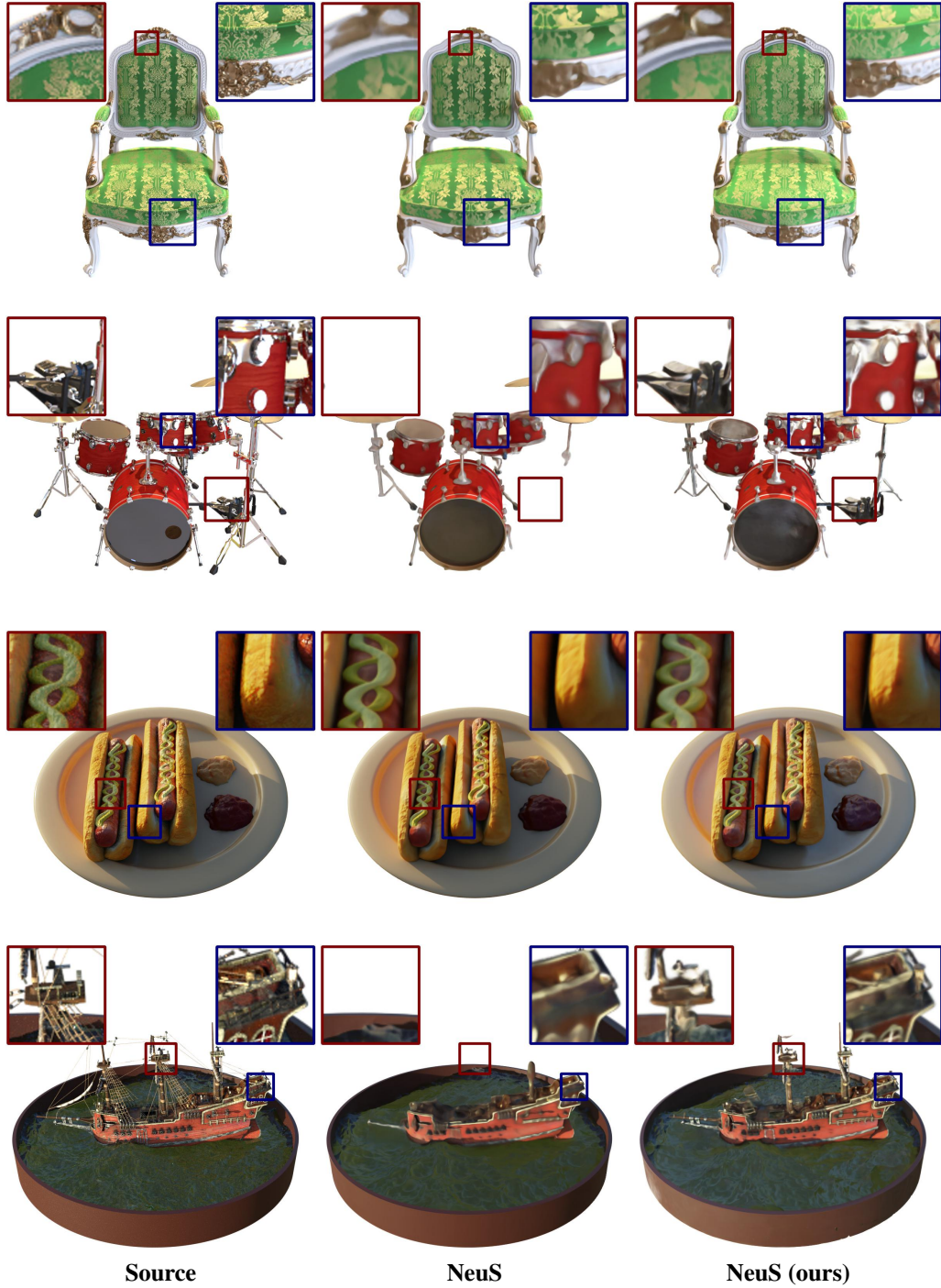


Figure 18: Rendering results on the Realistic Synthetic 360 dataset [20] for NeuS [31] method.

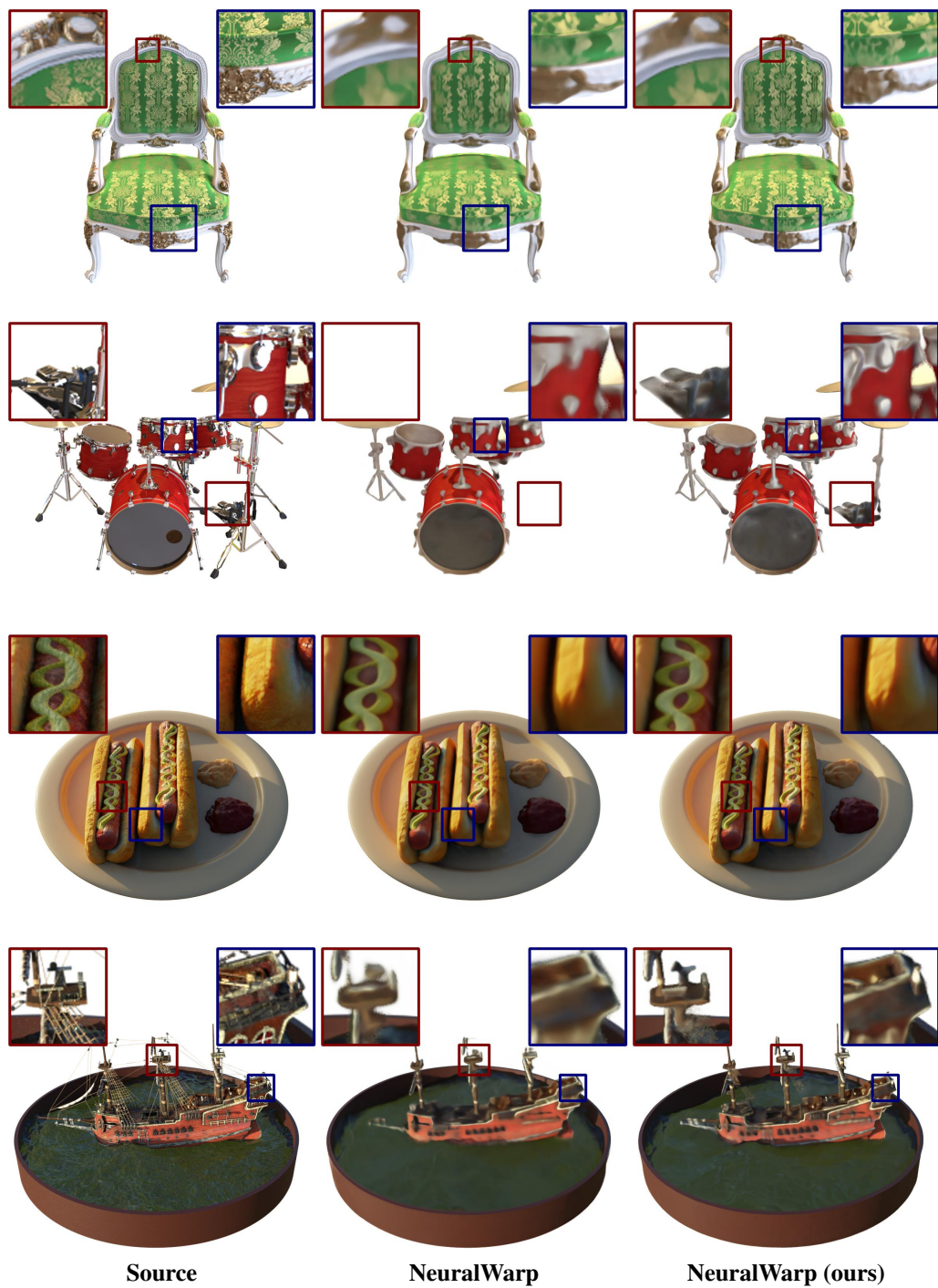


Figure 19: Rendering results on the Realistic Synthetic 360 dataset [20] for NeuralWarp [4] method.

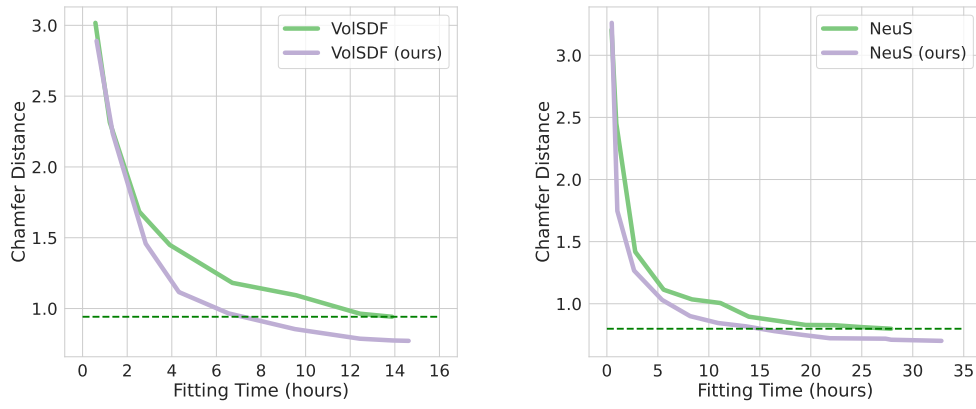


Figure 20: Chamfer Distance vs training speed comparison. The Chamfer Distance is computed with the standard evaluation protocol and averaged across the 15 scenes in the DTU benchmark. We train the NeuS-based [31] models for 300k iterations and the VoISDF-based [38] models for 100k iterations as in the reference publications. The models were trained using NVIDIA P40 GPUs. Our proposed approach has a per-iteration overhead of 10-20% depending on the scene and base method, yet converges faster to better Chamfer scores by requiring significantly fewer iterations.